Structure and mechanism of interleukin-1β converting enzyme

Keith P. Wilson, Jo-Anne F. Black, John A. Thomson, Eunice E. Kim, James P. Griffith, Manuel A. Navia, Mark A. Murcko, Stephen P. Chambers, Robert A. Aldape, Scott A. Raybuck & David J. Livingston

Vertex Pharmaceuticals Incorporated, 40 Allston Street, Cambridge, Massachusetts 02139, USA

Interleukin-1β converting enzyme (ICE) processes an inactive precursor to the proinflammatory cytokine, interleukin-1β, and may regulate programmed cell death in neuronal cells. The high-resolution structure of human ICE in complex with an inhibitor has been determined by X-ray diffraction. The structure confirms the relationship between human ICE and cell-death proteins in other organisms. The active site spans both the 10 and 20K subunits, which associate to form a tetramer, suggesting a mechanism for ICE autoactivation.

HUMAN interleukin-1β converting enzyme (ICE), a cysteine protease localized primarily in monocytes, processes the 33K inactive precursor of interleukin-1β (pIL-1β) to the 17K pro-inflammatory cytokine IL-1β (refs 1, 2). ICE has a unique sequence preference among mammalian proteases, and requires substrates with aspartic acid adjacent and n-terminal to the scissile peptide bond (P_1 residue)[3,4]. To date, pIL-1β is the only identified physiological substrate. pIL-1β lacks a conventional leader sequence and is not processed by a signal peptidase[5], nor directed to the Golgi apparatus for secretion[6]. Instead, pIL-1β is cleaved by ICE between Asp 116 and Ala 117 to produce the biologically active carboxy-terminal fragment found in human serum and synovial fluid[3,4]. Processing by ICE is necessary for transport of mature IL-1β through the cell membrane.

Active ICE is an oligomeric enzyme with subunits of relative molecular masses (M_r) of 20K and 10K, denoted here as p20 (residues 120–297) and p10 (317–404), respectively[7,8]. The subunits are derived from a 45K pro-enzyme (p45) by cleavage at four Asp–Xaa bonds, Asp 103–Ser 104, Asp 119–Asn 120, Asp 297–Ser 298, and Asp 316–Ala 317 (ref. 7). Purified p45, and the p30 form which lacks the amino-terminal pro sequence, can autoprocess to the active form *in vitro* by manipulation of enzyme concentration and temperature[7].

ICE or ICE homologues may regulate programmed cell death (apoptosis). ICE shares 28% sequence identity with CED-3, a *Caenorhabditis elegans* protein in the apoptosis pathway, and overexpression of murine ICE in *Rat-1* fibroblast cells causes cell death[9,10]. Increased ICE activity has been reported in phagocytic cells stimulated with agents which promote apoptosis[11]. The *crmA* protein, a viral serpin inhibitor of ICE[12], protects transfected ganglion neurons from apoptosis induced by nerve growth factor depletion[13]. These observations suggest that programmed cell death observed in degenerative neuronal diseases, such as Alzheimer's and Parkinson's diseases[14], may be regulated by ICE or ICE homologues.

We have solved the structure of ICE at 2.6 Å resolution by X-ray diffraction (Table 1). Structural, kinetic and mutagenesis data suggest mechanisms for ICE catalysis and regulation.

Fold and topology of ICE

Each ICE heterodimer resembles a rectangular box with rough dimensions 45 Å × 35 Å × 25 Å. The p20 and p10 subunits are intimately associated, and the protein appears as a single domain (Fig. 1). The enzyme core is a six-stranded β-sheet with five parallel strands (1, residues 164–170; 2, 199–205; 3, 230–236; 4, 278–283; and 7, 327–331) and one anti-parallel strand (8, residues 388–393). The anti-parallel strand lies on one edge of the sheet, and is perpendicular and adjacent to the crystallographic 2-fold axis. Six α-helices (A, residues 139–149; B, 182–196; C, 207–226; D, 257–269; E, 348–363; and F, 366–377) lie roughly parallel to the β-strands and shield the β-sheet core from solvent. The last seven residues of p20 and the first seven of p10 protrude from this compact structure and form two anti-parallel β-strands (5, residues 291–297 and 6, 317–323) that interact extensively across the 2-fold axis of the crystal (Fig. 2).

The active site

We solved the structure of ICE bound to a tetrapeptide aldehyde inhibitor (acetyl-Tyr-Val-Ala-Asp-H)[15] to suppress autoproteolysis at the protein concentrations used for crystallization. The inhibitor is covalently bound to the sulphur atom of Cys 285 (Fig. 4*a*). Other cysteine-modification agents are selective for Cys 285 (ref. 7). In concert with the site-directed mutagenesis experiments reported here (Fig. 3), Cys 285 is confirmed as the active site nucleophile. The His 237 imidazole side chain is adjacent to Cys 285 (Fig. 4*a*) and participates in a hydrogen-bond network that includes the oxyanion of the aldehyde inhibitor, suggesting a role for this residue in catalysis.

The structure of the inhibited complex reveals why both p20 and p10 subunits are required for ICE activity[7]. The tetrapeptide inhibitor binds in the S_1 to S_4 ICE subsites which would contact peptide substrate residues N-terminal to the scissile peptide bond. Side chains from p10 form the S_2 to S_4 subsites (Fig. 4*b*). The inhibitor makes main chain to main chain contacts with residues from p10 in an anti-parallel β-sheet arrangement (Fig. 4*b*). The side chains of p10 residues Val 338 to Pro 343 interact with the inhibitor, except for Ser 339, whose side chain is buried in the protein core. The γ-oxygen of Ser 339 is near the sulphur atom of Cys 285 (3.9 Å), and is stabilized by the side-chain oxygen atoms of two other buried Ser residues (332 and 333) and a water molecule. Both subunits contribute to the selective aspartic acid recognition by the S_1 subsite[7], through direct charge–charge interactions with the side chains of Arg 179 (p20) and Arg 341 (p10). On the basis of hydrogen bonding distances and geometry, the more important interaction is with residue Arg 179 (Fig. 4*a*). The side chain NH of Gln 283 also hydrogen bonds to the P_1 carboxylate side chain of the inhibitor. The Ala side chain at P_2 and the Val at P_3 of the inhibitor are exposed to solvent (Fig. 4*b*), consistent with the broad tolerance of substitution in the P_2 position of substrates[7]. The Tyr side chain in P_4 contacts the

FIG. 1 Stereo ribbon[43] drawing of the p20 (blue)p10 (red) ICE heterodimer. Secondary structural elements are labelled (gold lettering) as defined in the text. The placement and orientation of secondary structural elements in ICE is similar to a portion of horse liver alcohol dehydrogenase and thioredoxin[44,45]. A few key residues referred to in the text are labelled (green lettering) according to their position in the p45 amino-acid sequence of ICE[7,8]. The locations of site-directed mutants discussed in this report are highlighted (green backbone) and have their side chain atoms displayed. The active site is at the top of the figure, roughly at the centre of the cluster of displayed side chains. The side chains of His 237 and the catalytic Cys 285 are coloured purple. From left to right across the top of the figure are His 248, Cys 244, His 237, Arg 179, Cys 285 and the serine triplet, Ser 332, Ser 333 and Ser 339 (closest to Cys 285). A disulphide bond between Cys 136 from p20 and Cys 362 from p10 is observed (shown at lower right). Cys 136 is conserved in the murine and rat ICE sequences, but Cys 362 is not. Because disulphide bonds in cytoplasmic proteins are rare, this covalent modification may be an artefact of purification, refolding or crystallization. Mutation of ICE residue Cys 136 or Cys 362 to Ser maintains enzymatic activity, demonstrating that disulphide bond formation is not essential for enzymatic activity (Fig. 3).

side chains of His 342, Val 348 and Arg 383 (Fig. 4*b*), but it is not hydrogen bonded to the enzyme. Modelling studies indicate that the C-terminal region of substrate would contact p20 residues exclusively (in the S_1' to S_4' subsites).

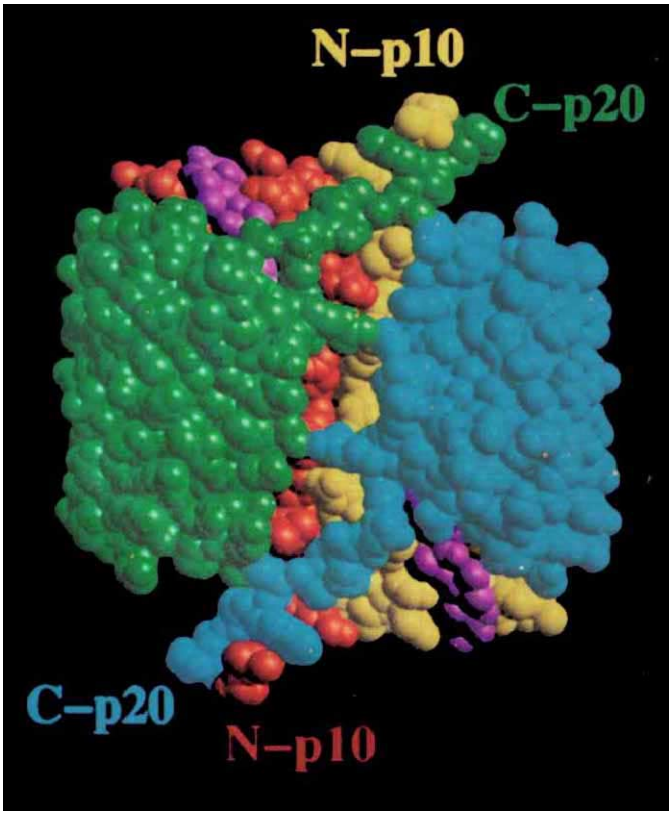

FIG. 2 CPK model of the $(p20)_2/(p10)_2$ tetramer of ICE. Two p20 subunits (green and blue) surround two adjacent p10 subunits (red and gold). The tetrapeptide aldehyde inhibitor is coloured purple. The crystallographic 2-fold axis is roughly perpendicular to the plane of drawing, and runs through the small hole at the centre of the interface between the two p10 subunits. Beta-strands 5 and 6 protrude from the top, and by 2-fold symmetry, from the bottom of the model. The N- and C-terminal end of each subunit is labelled. Dynamics simulations suggest that formation of a tetramer would stabilize the active site of ICE by reducing the mobility of the catalytic Cys 285 and other residues near the p20 C-terminus (D. Pearlman and M.A.M., unpublished results).

A second Cys/His pair (Cys 244–His 248) is found near the active site. The side chains of these two residues are in van der Waals contact, and these residues may contact the P_2' and P_3' side chains of substrates. Cys 244 also contacts His 237, the active site His. Together, the four residues are arranged in a side-by-side manner, Cys-His-Cys-His (Fig. 1). There is no evidence that these residues coordinate divalent metal ions, but thimerosal, a Hg compound, modifies Cys 244 in the presence of the aldehyde inhibitor and is a 15 μM uncompetitive inhibitor of ICE activity.

On the basis of an alignment of the ICE sequence Gly 287-Asp-Ser-Pro-Gly 291 to a consensus sequence in serine and viral cysteine proteases, it was suggested that Ser 289 might play a catalytic role in ICE[7]. The structure, however, shows that these residues form a turn near the C terminus of p20 and are not involved in catalysis. Mutation of Gly 287 to Ser eliminates the ability of murine ICE to induce apoptosis[9]. Both Gly residues of this pentapeptide have $\phi\psi$ angles that are excluded for amino acids with bulkier side chains. Gly 287 may also be involved in recognition of the P′ end of substrate. Thus, substitution at Gly 287 is likely to disrupt the structure near the active site.

Mutational and kinetic analysis of the active site

Inhibitors are used routinely to assign proteases to mechanistic classes, but ICE is not easily categorized in this way. Cys modification reagents such as pCMB, iodoacetate[7] and iodoacetamide[16], and the His modification agent DEPC (diethyl pyrocarbonate), inactivate ICE, and substrate protects against inactivation by these compounds (data not shown). These results suggest a role for active site Cys and His residues. Yet ICE is insensitive to several classic cysteine protease inhibitors, such as E64 and antipain. ICE is also inactivated by TPCK (*N*-tosyl-L-phenylalanine chloromethyl ketone) and 3,4-dichloroisocoumarin, reagents considered to be selective for serine proteases. Taken together, these observations suggest differences in the binding sites of ICE and papain, the latter a well-studied cysteine protease of known structure with high sequence similarity in the active site region to the human cysteine proteases cathepsin B and H (ref. 17).

To explore further the roles of ICE active site residues in substrate binding and catalysis, we investigated the ability of a series of p30 ICE mutants to process pIL-1β *in vivo* (Fig. 3). We transfected each ICE mutant into a COS cell line that constitutively expresses pIL-1β, and measured the amount of mature IL-1β secreted. Enzymatic activity in this assay requires that transcription, translation and protein folding of mutants are not arrested. We determined, therefore, the amount of mutant ICE

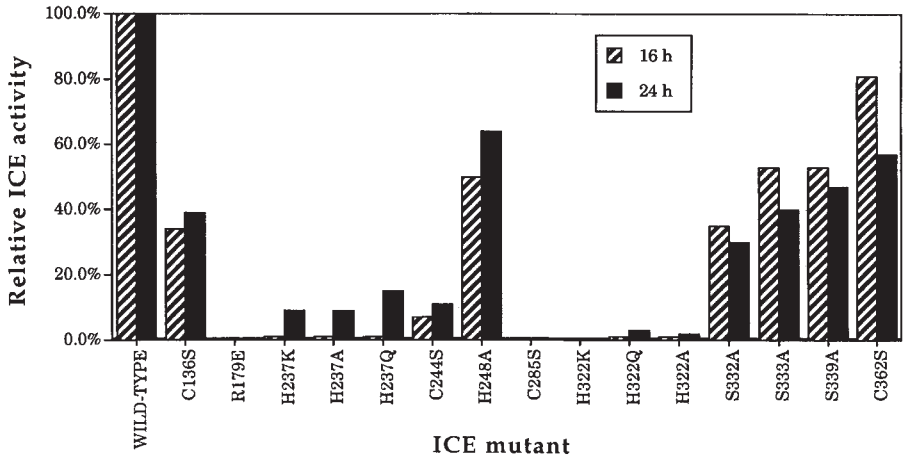

FIG. 3 Activity of ICE mutants in processing pIL-1β in COS-1 cells relative to wild-type activity. Mutations were made in the 30K ICE-encoding cDNA cloned into a pcDNA3 mammalian expression vector (Invitrogen) by oligonucleotide-directed mutagenesis, and fully sequenced in the coding region. The COS-1 cell line had been previously transfected with pIL-1β encoding cDNA which had integrated into the chromosome. pIL-1β production from COS-1 cells was maintained by the addition of 0.5 mg ml^{-1} G-418 sulphate to culture media. About 3×10^6 COS-1 cells in 100-mm tissue culture plates were transfected with 15 μg of each plasmid. DNA was mixed with 200 μl DEAE–Dextran, brought to 4 ml with phosphate-buffered saline, and added to the plates. Cells were incubated at 37 °C for 30 min. 8 ml of an 80 μM chloroquine/serum-free DMEM solution was added and cells were incubated for 2.5 h. This solution was aspirated and cells were treated for 2 min with 10% DMSO/serum-free DMEM. After washing with serum-free media, 10 ml complete media was added. Conditioned media were sampled at 16 (hatched bars) and 24 h (black bars). Detection of mature pIL-1β in the cell medium was accomplished by ELISA (R&D Systems). Media samples were diluted to achieve concentrations in the linear range of the ELISA assay (8–60 pg ml^{-1}). Background IL-1β concentrations were determined in media from cells transfected with the expression vector lacking ICE cDNA, and this value was subtracted from all other concentrations. The per cent activity values were calculated as the ratio of secreted IL-1β from cells transfected with mutant ICE divided by IL-1β secreted by cells transfected with wild-type ICE. Ratios are the means determined in at least two experiments.

present in cell lysates by western blotting using an anti-p20 rabbit antiserum, which also recognizes the intact p30 precursor. Similar amounts of p30 were observed for each mutant regardless of enzymatic activity, suggesting that even inactive mutants are efficiently transcribed, translated and folded (data not shown). Inactive mutants such as Cys 285 to Ala and His 237 to Ala can be distinguished, however, from active mutants by the lack of a p20 species in the former, demonstrating that autoprocessing has been abrogated by these mutations.

Using the transient expression system, we determined that

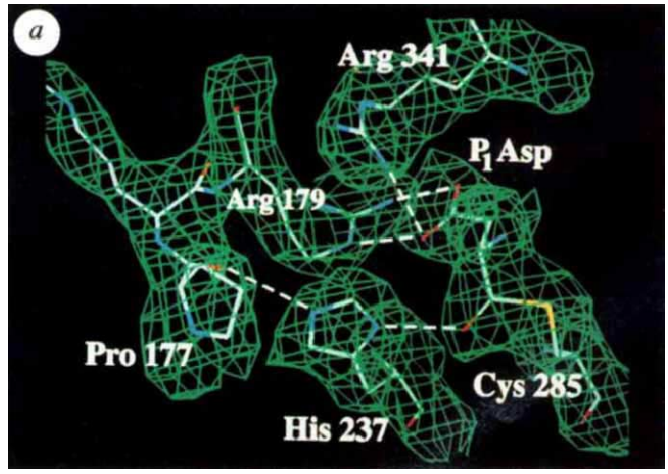

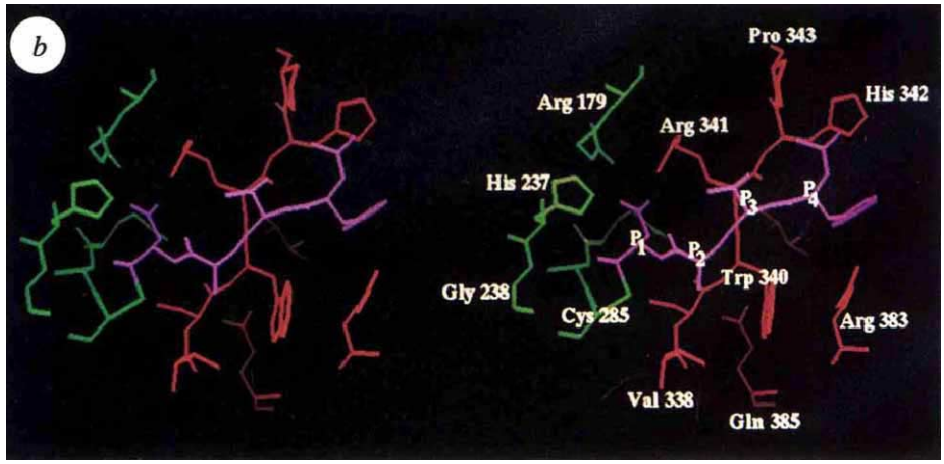

FIG. 4 *a*, Electron density map of the active site. The $|2F_{obs} - F_{calc}|$ Fourier synthesis was calculated at 2.6 Å resolution with phases determined from the refined coordinates. The contour level is $+0.8\sigma$, where σ is the root-mean-square density throughout the unit cell. The refined coordinates of the final model are superimposed and identified by their three-letter codes and by sequence position. Carbon atoms are coloured white, nitrogen atoms blue, oxygen red and sulphur is yellow. Hydrogen bonds are depicted as dashed lines. *b*, Stereo stick drawing of the active site. Residues of ICE in contact with the tetrapeptide aldehyde inhibitor (coloured purple) are coloured by subunit, with p20 residues coloured green and p10 residues red. Residues of ICE that have at least one atom within 4 Å of any atom in the inhibitor are; Arg 179; Ser 236; His 237; Gly 238; Gln 283; Ala 284; Cys 285; Val 338; Ser 339; Trp 340; Arg 341; His 342; Pro 343; Met 345; Val 348; and Arg 383. The acetyl group of the inhibitor is adjacent to Pro 343. Definitions: P4, tyrosine; P3, valine; P2, alanine; P1, aspartic acid.

TABLE 1 Structure determination of ICE

Protein modification	Resolution (Å)	Completeness of data (%)	R_{merg}* (%)	Unit cell dimensions (Å) a, b	Unit cell dimensions (Å) c	No. of sites	R_c* (%)	Phasing power*
Tetrapeptide aldehyde†	20–2.6	90	8.3 (2)	64.4	163.3	—	—	—
Tetrapeptide aldehyde	20–2.8	78	8.3 (3)	64.7	162.9	—	—	—
Iodinated tetrapeptide aldehyde	20–3.5	86	9.4 (2)	64.4	162.8	2	0.88	1.09
Thimerosal	20–3.5	88	8.4 (1)	64.4	162.3	5	0.67	1.08
Gold thiomalate	20–3.5	74	9.5 (1)	64.7	162.7	3	0.72	1.22
Uranyl acetate	20–4.0	80	10.8 (2)	64.7	162.9	2	0.79	1.32
Lead chloride	20–3.5	64	8.9 (2)	64.7	162.8	2	0.76	1.38

Details of the expression, purification, autoprocessing, and sample preparation for crystallization will be published elsewhere (J.A.T. *et al.*, manuscript in preparation). Crystals of inhibited ICE were grown by vapour diffusion. Protein (20 mg ml^{-1} in 50 mM citrate, 2.0 mM DTT, pH 6.5) was mixed with reservoir (15% PEG 4K, 400 mM $LiSO_4$, 200 mM sodium HEPES, 5 mM sodium cacodylate, 0.5% beta-octyl glucoside, pH 7.0) and allowed to stand over the reservoir solution at 4 °C. Crystals were equilibrated with 18% PEG 4K reservoir solution before data collection or derivatization. Refined heavy-atom parameters were used to compute multiple isomorphous replacement phases. The mean figure of merit was 0.65 to 3.5 Å resolution. Including the anomalous data for the Hg derivative showed the space group to be $P4_32_12$ rather than its enantiomorph. The initial electron density map revealed the beta-sheet and five of the surrounding helices. Solvent flattening and phase extension[38] improved the map, and was followed by cycles of model building[39], positional refinement[40,41], and phase combination[38] until the switch to phases calculated from the model could be made. The current model is consistent with the derived amino-acid sequence of ICE[7,8] and the chemical nature of the heavy-atom substitutions. The model has an *R*-factor of 19% against all observed data between 7 Å and 2.6 Å resolution, with root-mean-square deviation from ideal bond lengths and angles of 0.010 Å and 2.82°, respectively. We see no electron density for amino acids 120 to 130, and they are presumed disordered. We have confirmed their presence in the crystal by amino-acid sequence analysis. Atomic coordinates for ICE will be submitted to the Brookhaven Protein Data Bank.

* See ref. 42 for definitions.

† Data collected at −6 °C.

mutation of Cys 285 or His 237 eliminates pIL-1β processing activity (Fig. 3) as well as autoprocessing, confirming their role in catalysis. Mutation of Arg 179, which contacts the P_1 Asp, to Glu also abolishes activity. Each of these active site residues is conserved in the human, murine and rat ICE complementary DNA sequences[7,8,18,19], as well as in three *ced-3* sequences[9]. Mutation of Cys 244 to Ala, which may contact P′ side chains of substrates, reduces enzymatic activity significantly (Fig. 3). In contrast, mutation of other residues proximal to Cys 285 does not eliminate activity. Such residues include Ser 332, 333 or 339, and His 248, which are not conserved in *ced-3* sequences[9].

The pH dependence of ICE enzymatic activity (k_{cat}/K_m) fits a sharp bell-shaped curve with a maximum at pH 7.5, with component pK_as of 5.5 and 8.2. The basic limb of the pH dependence is consistent with protonation of a weak base such as His 237, which may function as a general acid-base during catalysis[20,21] and/or increase binding affinity of substrate. The turnover number (k_{cat}) of ICE is low, about 1 s^{-1} for the tetrapeptide *p*-nitroanilide substrate, compared to 42 s^{-1} for papain for a dipeptidyl *p*-nitroanilide substrate[22]. ICE lacks a polarizing acidic residue in the active site, corresponding to papain Asp 158. This difference may help explain the low k_{cat} of ICE, which is comparable to those observed for Asp 158 mutants of papain[23].

ICE is a $(p20)_2/(p10)_2$ tetramer

ICE has been described as a heterodimer[7], but the arrangement of p20 and p10 subunits in the crystal shows that ICE is a tetramer (Fig. 2). Two p20 subunits (green and blue) surround two adjacent p10 subunits (red and gold) that interact across the crystallographic 2-fold axis. The area of contact buried in this interface between p10 subunits is ~5,200 Å^2. In comparison, the surface area buried between subunits of proteins in the 24–40K range that form dimers is often ~1,800 Å^2 (ref. 24). This observation suggests that the crystallographic 2-fold axis corresponds to an oligomer interface solution, and that ICE is a $(p20)_2/(p10)_2$ tetramer.

Other evidence supports this hypothesis. Sequence comparison between human and murine ICE[18] reveals that p10 is more highly conserved (81%) than p20 (59%). Much of the dimer–dimer interface consists of p10 residues 318–322 and 386–396. Thirteen of these sixteen residues are conserved, consistent with their location at the proposed tetramer interface. Four of the six residues from the p20 subunits that make contacts across the 2-fold axis are also conserved. Mutation of His 322, a residue 35 Å away from the active site, to Ala, Lys or Gln eliminates ICE activity (Figs 1 and 3). Sensitivity to substitution at this residue is consistent with the higher association state we propose, where His 322 is completely buried in the interface between the p10 subunits. In solution, we have analysed the distribution of ICE $(p20)_n/(p10)_n$ oligomers by size-exclusion chromatography and by quasi-elastic light scattering. A continuous distribution of ensembles up to very high molecular mass aggregates ($M_r > 10^6$), which may include a tetrameric species, is observed (data not shown).

The quaternary arrangement of p20/p10 subunits (Fig. 2) raises the question of which pair of subunits originates from a contiguous p45 percursor polypeptide. If we consider an ICE p20/p10 dimer (the green/red or the gold/blue pair in Fig. 2) to be derived from one p45 molecule, then the measured distance from the α-carbon of the p20 C-terminal residue (Asp 297) to the α-carbon of the N-terminal p10 residue (Ala 317) is 67 Å. This distance would have to be spanned by the 19 amino acids removed during processing of ICE to its active form. This possibility seems unlikely unless large conformational changes accompany autoprocessing. Alternatively, we propose that an ICE p20/p10 dimer is derived from two different p45 molecules, that is, the green/gold pair (or the blue/red pair) in Fig. 2 arises from the same p45 precursor. In this model, the distance between the α-carbons of Asp 297 and Ala 317 is 4.9 Å, and the residues preceding these form two anti-parallel β-strands that include six main-chain hydrogen bonds. A salt bridge between the p20 C terminus and the p10 N terminus is observed, and would be generated after p45 is processed to the active form.

Discussion

ICE defines a new class of cysteine proteases with respect to global fold, topology, and quaternary structure. The topology of ICE is different from cysteine proteases in the papain subfamily. The papain active site cysteine residue is located at the N terminus of an α-helix, whereas Cys 285 of ICE is at the C-terminal end of β-strand 4. ICE is more closely related to the recently discovered CED-3 protein[9]. Residues 246–320 of CED-3 share 43% sequence identity with residues 166–287 of human ICE[9]. This region of ICE includes all of the residues important for recognition of aspartic acid in P_1 (Arg 179, Gln 283) and for

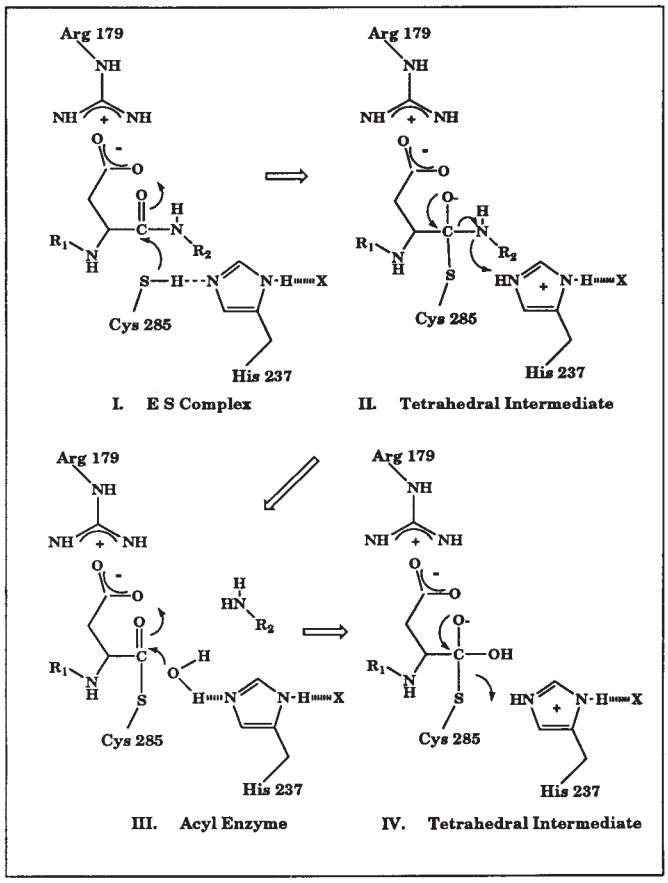

FIG. 5 A plausible mechanism for ICE catalysis of peptide hydrolysis using the Cys 285–His 237 catalytic diad. For the synthetic substrate used to quantify ICE activity, R_1 represents a Suc-Tyr-Val-Alanyl tripeptide and R_2 represents a *p*-nitrophenyl group. The structure of the peptide–aldehyde complex does not identify unambiguously a putative third residue (X) that would enhance the basicity of the His 237 imidazole ring by hydrogen bonding. The identity of this residue would vary depending on the torsion angles of the His 237 side chain in the enzyme–substrate complex. In the appropriate geometry, X might represent the carbonyl oxygen of Pro 177 or the P_1 carboxylate oxygen of substrate. The Arg 341 guanidino group may also be involved in electrostatic interactions with the substrate P_1 carboxylate.

catalysis (His 237 and Cys 285). These residues are all conserved in CED-3, suggesting that *ced-3* genes encode ICE-like cysteine proteases[9].

The hydrolytic mechanism of ICE must proceed through formation of a substrate tetrahedral intermediate, probably requiring activation of the Cys 285 side chain by polarization and/or deprotonation by His 237 in a catalytic diad (Fig. 5). Two possible geometries for a substrate tetrahedral intermediate are suggested by the structure. In one, the oxyanion points away from the Cys 285 backbone amide and is in contact with the imidazole ring of His 237. This model is consistent with the structure reported here for the peptide aldehyde complex (Fig. 4*a*), but may be the opposite geometry of the enzyme–substrate tetrahedral intermediate. More likely, the oxyanion of the substrate tetrahedral intermediate interacts with the backbone amide protons of Cys 285 and Gly 238, which do not have hydrogen-bonding partners in the structure of the ICE–aldehyde complex. In this geometry, His 237 participates in general acid catalysis of acyl-enzyme formation by protonation of the tetrahedral intermediate aminol nitrogen atom (Fig. 5). Depending on the torsion angles of the His 237 side chain, atoms such as the carbonyl oxygen of Pro 177, or perhaps the substrate P_1 carboxylate oxygen, may orient His 237 during catalysis.

We propose that the active form of ICE in solution is a tetramer of interdigitating subunits, a unique quaternary structure among known proteases. A tetrameric association state has implications for ICE autoprocessing and regulation. In the tetramer, the p10 subunit from one ICE molecule complexes with the p20 subunit from a different molecule to create an active site. Two of the cleavage sites required to generate active ICE are located adjacent in space in this arrangement, and share a surface-exposed location that would aid processing.

ICE activity may be regulated allosterically because enzymatic activity is sensitive to mutations at the dimer–dimer interface, far removed from the active site (Figs 1 and 3). We have identified two non-competitive inhibitors of ICE, gold-thiomalate and auranofin, which are anti-inflammatory agents that are known to decrease circulating IL-1β levels[25]. Gold-thiomalate binds to Cys 364 and Cys 397, residues distant from the active site (~30 Å), and located adjacent to the 2-fold axis in the crystal (Table 1). Auranofin binds equally well to Cys 364 (data not shown). It is possible that the interface between ICE p10 subunits is a physiological target for these compounds.

The high-resolution structure of ICE we describe will accelerate efforts to design specific inhibitors of ICE. Elevated levels of IL-1β have been detected in septic shock, rheumatoid arthritis, diabetes and other autoimmune diseases[26–30]. Inhibition of IL-1β activity has been demonstrated to ameliorate symptoms in several animal models of human inflammatory disease[31–35]. IL-1β is also overexpressed in the brain of patients with Alzheimer's disease[36], and a recently reported clinical trial with Alzheimer's patients suggests that anti-inflammatory drugs may be preventative[37]. ICE inhibitors may constitute a new type of anti-inflammatory agent, and ultimately find use in therapy of inflammation and neurodegenerative diseases. □

Received 4 March; accepted 23 June 1994.

1. Black, R. A., Kronheim, S. R. & Sleath, P. R. *FEBS Lett.* **247,** 386–390 (1989).
2. Kostura, M. J. *et al. Proc. natn. Acad. Sci. U.S.A.* **86,** 5227–5231 (1989).
3. Sleath, P. R., Hendrickson, R. C., Kronheim, S. R., March, C. J. & Black, R. A. *J. biol. Chem.* **265,** 14526–14528 (1990).
4. Howard, A. D. *et al. J. Immun.* **147,** 2964–2969 (1991).
5. March, C. J. *Nature* **315,** 641–647 (1985).
6. Singer, I. I. *et al. J. exp. Med.* **167,** 389–407 (1988).
7. Thornberry, N. A. *et al. Nature* **356,** 768–774 (1992).
8. Cerretti, D. P. *et al. Science* **256,** 97–100 (1992).
9. Yuan, J., Shaham, S., Ledoux, S., Ellis, H. M. & Horvitz, H. R. *Cell* **75,** 641–652 (1993).
10. Miura, M., Zhu, H., Rotello, R., Hartweig, E. A. & Yuan, J. *Cell* **75,** 653–660 (1993).
11. Nett-Fiordalisi, M. A., Berson, D. R. & Chaplin, D. D. *J. Cell Biochem.* **17B,** 117 (1993).
12. Ray, C. A. *et al. Cell* **69,** 597–604 (1992).
13. Gagliardini, V. *et al. Science* **263,** 826–828 (1994).
14. Marx, J. & Barinaga, M. *Science* **259,** 760–762 (1993).
15. Chapman, K. T. *Biorg. med. Chem. Lett.* **2,** 613–618 (1992).
16. Miller, D. K. *et al. Ann. NY Acad. Sci.* **696,** 133–148 (1993).
17. Kamphuis, I. G., Drenth, J. & Baker, E. N. *J. molec. Biol.* **182,** 317–329 (1985).
18. Nett, M. A. *et al. J. Immun.* **149,** 3254–3259 (1992).
19. Shivers, B. D., Giegel, D. A. & Keane, K. M. *J. Cell Biochem.* **17B,** 119 (1993).
20. Polgar, L. *Eur. J. Biochem.* **33,** 104–109 (1973).
21. Baker, E. N. & Drenth, J. in *Biological Macromolecules and Assemblies* Vol. 3 (eds Jurnak, F. & McPherson, A.) 312–368 (Wiley, New York, 1987).
22. Menard, R. *et al. Biochemistry* **30,** 8924–8928 (1991).
23. Menard, R. *et al. Biochemistry* **30,** 5531–5538 (1991).
24. Miller, S., Lesk, A. M., Janin, J. & Chothia, C. *Nature* **328,** 834–836 (1987).
25. Bender, P. E. & Lee, J. C. *A. Rep. med. Chem.* **25,** 185–193 (1989).
26. Dinarello, C. A. *Immun. Rev.* **127,** 119–146 (1992).
27. Harris, E. D. Jr *New Engl. J. Med.* **322,** 1277–1289 (1990).
28. Mandrup-Poulsen, T. *et al. Cytokine* **5,** 185–191 (1993).
29. Hammerburg, C. *et al. J. clin. Invest.* **90,** 571–583 (1992).
30. Noronha, I. L., Kruger, C., Andrassy, K., Ritz, E. & Waldherr, R. *Kidney Int.* **43,** 682–692 (1993).
31. Dinarello, C. A., Gelfand, J. A. & Wolff, S. M. *J. Am. med. Ass.* **269,** 1829–1835 (1993).
32. Geiger, T. *et al. Clin. exp. Rheumatol.* **11,** 515–522 (1993).
33. Ohlsson, K., Bjork, P., Bergenfeldt, M., Hageman, R. & Thompson, R. C. *Nature* **348,** 550–552 (1990).
34. Wooley, P. H. *et al. Arthritis Rheumatol.* **36,** 1305–1314 (1993).
35. Sandberg, J-O., Eizirik, D. L., Sandler, S., Tracey, D. E. & Andersson, A. *Diabetes* **42,** 1845–1851 (1993).
36. Griffin, W. S. T. *et al. Proc. natn. Acad. Sci. U.S.A.* **86,** 7611–7615 (1989).
37. Breitner, J. C. S. *et al. Neurology* **44,** 227–232 (1994).
38. CCP4-Collaborative Computing Project No. 4 *A Suite of Programs for Protein Crystallography* (Daresbury Laboratory, Warrington, 1979).
39. *Quanta* version 4.0b (Molecular Simulations Inc., Burlington MA, 1992).

40. Brünger, A. T. *Acta crystallogr.* **A46,** 46–57 (1990).
41. Brünger, A. T., Krukowski, A. & Erickson, J. *Acta crystallogr.* **A46,** 585–593 (1990).
42. Blundell, T. L. & Johnson, L. N. *Protein Crystallography* (Academic, New York, 1976).
43. Carson, M. *J. appl. Crystallogr.* **24,** 958–961 (1991).
44. Eklund, H. *J. molec. Biol.* **102,** 27 (1976).
45. Holmgren, A., Soderberg, B.-O., Eklund, H. & Branden, C.-I. *Proc. natn. Acad. Sci. U.S.A.* **72,** 2305–2309 (1975).

ACKNOWLEDGEMENTS. We thank T. Fox and J. Coll for assistance with protein purification and chemical modification studies, M. Mullican, D. Lauffer and T. Tung for synthesis of the inhibitors used in the structure determination, O. Futer for assistance with mutagenesis, J. Fulghum for assistance with fermentation, M. Fleming for protein sequence analysis and oligonucleotide synthesis, G. Bemis and D. A. Pearlman for molecular dynamics analysis and discussions on mechanism, M. D. Sintchak for help with figures and J. Boger and V. Sato for reading of the manuscript.

LETTERS TO NATURE

Stars within the Large Magellanic Cloud as potential lenses for observed microlensing events

Kailash C. Sahu

Instituto de Astrofisica de Canarias, 38200 La Laguna, Tenerife, Spain

MASSIVE compact objects in the Galactic halo, known as MACHOs, have been postulated as the origin of a substantial fraction of the 'dark matter' known to exist in the haloes of galaxies[1,2]. Paczyński[3] has suggested that it might be possible to detect these low-luminosity objects by their potential to act as gravitational lenses, causing a characteristic brightening when they cross the path of light from a star in a nearby galaxy. Very recently, two groups reported possible detections of microlensing of stars in the Large Magellanic Cloud (LMC)[4,5], which was interpreted as a possible fingerprint of MACHOs. Here I show that microlensing by stars within the LMC itself can account for the observed events. In the future it should be possible to distinguish between the two possible sources of microlensing events, however, because events caused by stars in the LMC should be clustered toward the central region of that galaxy whereas those caused by MACHOs should be uniformly distributed over the whole LMC.

Based on a suggestion by Paczyński[3], two groups (involved in the monitoring of a few million stars in the LMC for more than a year) have reported the detection of three microlensing events as evidence for the presence of dark objects in the Galactic halo[4,5]. But this has also been the cause for some concern: if these events are caused by such objects in the halo, it would lead to some problems in terms of stellar evolution and the theory of galaxy formation[6]. Recent work on deuterium abundance derived from the observations of a quasar suggests that the dark haloes of galaxies may well be non-baryonic[7]. Furthermore, the rate of microlensing events as observed seems to be lower than expected for the dark halo, and it is important to estimate the rate expected from the stars that are known to exist in our Galaxy and in the LMC. The analysis for the Galactic stars has been done by Gould *et al.*[8], but the importance of the LMC stars has been overlooked so far although Gould[9] has investigated the possibility that MACHOs in the halo of the LMC might be the lenses. Here I present an estimate of the rate of microlensing events to be expected from the LMC stars acting as gravitational lenses.

To calculate the probability of the microlensing being caused by a star in the LMC itself, we need to know the stellar mass density there. First, I consider only the bar of the LMC. From the surface luminosity, it is estimated that the observed luminosity of the bar is ~10–12% of the total observed luminosity of the LMC in the optical wavelengths[10,11]. To calculate the extinction, I have used the IRAS 100-μm maps[12,13], the background galaxy counts[14], and the observations of the most reddened stars in the region[15], which together give a consistent value of 1.5 mag in the V band. To see how the extinction affects the mass, I assume that the extinction is uniform in depth. Thus for any line of sight, if A_v is the total extinction in the line of sight, then the ratio of the observed to true luminosity at any point

$$\frac{L_{obs}}{L_{true}} = \frac{1}{d}\int_0^d 2.5^{-A_v l/d}\,dl = \frac{1-e^{-0.916A_v}}{0.916A_v} \qquad (1)$$

where d is the total depth and l corresponds to the direction of the line of sight. Using $A_v = 1.5$ mag for the bar, and $A_v = 0.3$–0.4 mag for the region outside, it is easy to show that the true luminosity of the bar is ~14–18% of the total luminosity of the LMC. The total mass of the LMC, as determined from various methods, is in the range $(6–15) \times 10^9 M_\odot$ (refs 10, 16) where $M_\odot$ is the solar mass. Assuming that the mass-to-light ratio in the bar and the outer parts are the same, the mass of the bar can be taken as $2 \times 10^9 M_\odot$. Considering the fact that the LMC is gas-poor and only ~5% of the LMC mass is neutral hydrogen[16–18], I will neglect the contribution of gas to the mass and assume that the entire mass is made up of stars.

To calculate the probability of microlensing, I assume that there are N_{tot} stars being monitored. To determine the effect of extinction on the number of monitored stars at various depths, I note that the limiting magnitude of the current surveys are ~20–21, which at the distance of the LMC, corresponds to an absolute magnitude of 1.5–2.5. So the magnitude of the stars that can be observed at the near side is 1.5 to 2.5, whereas the limiting magnitude at the far end is 1.5 mag brighter. If the distribution of stars among different spectral types is assumed to be similar to that observed in the solar neighbourhood, then the difference in the monitored number of stars per unit depth from front end to the back is ~3 (ref. 19). (As it turns out, the effect of extinction is small. If the extinction is 3 instead of 1.5 mag, the net probability decreases only by <50%.)

Hence assuming the extinction to be uniform in depth, the observed number of stars at any layer dl, at a depth of l, can be expressed as

$$N_{obs}(l) = N_1 3^{-l/d}\,dl \qquad (2)$$

where N_1 is the observed number of stars per unit depth in absence of extinction. If N_{tot} is the total number of stars being monitored, then

$$N_{tot} = \int_0^d N_1 3^{-l/d}\,dl = 0.6 N_1 d \qquad (3)$$

Substituting equation (3) in equation (2)

$$N_{obs}(l) \approx \frac{N_{tot}}{0.6d} 3^{-l/d}\,dl \qquad (4)$$

The fraction of area covered by the Einstein rings of all the individuals stars lying in the front of this layer can be expressed as

$$A_f(l) = \int_0^l \pi R_E^2(l) n(l)\,dl \qquad (5)$$

where $n(l)$ is the stellar number density at depth l and R_E is the Einstein radius. Note that $n = \rho/m$ and $R_E^2 \propto m$ where ρ is the